Actin network heterogeneity tunes activator-inhibitor dynamics at the cell cortex

Ondrej Maxian[1,2], Aaron R. Dinner[2,3,4], and Edwin Munro[1,2]

[1]Department of Molecular Genetics and Cell Biology,
[2]Institute for Biophysical Dynamics,
[3]Department of Chemistry, and
[4]James Franck Institute, University of Chicago, Chicago IL, 60637

Abstract

Biological systems can display diverse patterns of self-organization, even when built on conserved networks of interaction between molecular species. In these cases, reaction-diffusion equations provide a valuable tool to learn how new dynamics could emerge from quantitative tuning of parameters. Bringing these models into quantitative correspondence with biological data remains an outstanding challenge, especially when the biology manifests heterogeneities that are difficult to account for mathematically. One particular example occurs in cell biology, where the membrane-bound regulatory protein RhoA interacts with the filamentous actin cortex in an activator-inhibitor loop. Though this core biochemical circuit is conserved across multiple cell types in different organisms, it produces different patterns of RhoA activity in different contexts, from traveling waves in starfish to transient pulses in *C. elegans*. To understand how this variation emerges, we develop an activator-inhibitor model that accounts explicitly for actin assembly and heterogeneity. We use the model to infer the parameters of actin dynamics responsible for each experimental phenotype, and find them to agree with independent measurements in most cases. To interpret parameter groupings, we use a simplified model to demonstrate how spatial and orientational randomness separately induce variation in spatiotemporal dynamics of RhoA activity. This work sheds light on how phenotypic diversity arises from heterogeneity and anisotropy, with important implications for the next generation of activator-inhibitor models.

Significance. To divide, move, and polarize, cells must self-organize their constituent proteins into large-scale patterns with varied spatiotemporal character. The design principles of this process remain poorly understood, primarily because a quantitative match between mathematical models and experimental data is difficult. In this paper, we consider pattern formation from two constituents on the cell cortex: the regulatory protein RhoA, and actin filaments. Using a mathematical model, constrained quantitatively on data from multiple organisms, we show how diversity in RhoA activity patterns could arise from intra- and inter-organismal changes in actin filament architecture and assembly dynamics. Our results reveal general principles for pattern formation at the cortex, and our combination of data analysis, modeling, and parameter inference provides a broadly-applicable, interdisciplinary methodology to unravel self-organization.

Introduction

In cellular and developmental biology, large-scale patterns emerge from self-organization of small-scale constituents [1]: of molecules within cells [2–5] and cells within tissues [6, 7]. In cells in particular, the structure, function, and interactions of key proteins are often conserved, yet these

proteins can self-organize into different structures in different contexts [8,9], implying that variations in emergent patterns must come from quantitative differences in the underlying parameters of interaction. Understanding how molecular-scale parameter tuning contributes to cell- and tissue-scale variation remains challenging, however, both because of the difficulty of making direct parameter measurements *in vivo*, and because developmental patterning involves collective dynamics with complicated feedbacks. Consequently, mathematical models play an essential role in inferring how changes in parameters could produce new phenotypes.

Arguably the most influential class of developmental patterning models are Turing type activator-inhibitor models and more generally reaction-diffusion models [1,10–13]. These clearly demonstrate how changes in parameters (e.g., the diffusion constant of each species) can give rise to dramatically different spatial patterns of self organization (e.g., standing patterns and traveling waves) [13–18]. To date, however, these models have largely been used qualitatively, for instance to explore the emergence of patterns [5, 19–24] or differentiate mechanistic hypotheses [21, 25], rather than to fit data directly and infer parameter values [26–28]. The latter approach is more difficult because of the trade-off between model and experimental complexity; for robust inference, the model must be complex enough to describe all of the underlying experimental data, but simple enough to make the inverse problem well posed [29]. Because of this, parameters often represent effective interactions of many molecules, and inferred values cannot be compared directly with experimental measurements for validation [26, 30–33].

In this paper, we study a paradigmatic example of molecular self-organization in cells, the dynamic coupling of the small GTPase RhoA and the cortical actin cytoskeleton which lies just beneath the cell membrane (Fig. 1A). The actin cytoskeleton is a filamentous meshwork, with architecture set by a balance of assembly dynamics and active remodeling [34–42], while RhoA (hereon "Rho") is a molecular switch which cycles between an active state and inactive state on the membrane [43–46]. Active Rho promotes further activation of Rho through GTP exchange factors (GEFs), and engages downstream effectors, such as formin and profilin, to nucleate, polymerize, and crosslink actin filaments (F-actin) [43, 44, 47]. Once assembled, F-actin recruits inhibitors (GTPase-activating proteins, GAPs) to inactivate Rho [20, 48], closing a negative feedback loop, and completing the activator-inhibitor circuit (Fig. 1A).

While the core molecular components of this circuit are broadly conserved across model organisms [19,20,48], the spatiotemporal dynamics of Rho are qualitatively different in different contexts. In frog and echinoderm embryos [19, 20, 49–52], traveling waves of Rho activity are observed, consistent with theoretical expectations for a rapidly-diffusing activator. In worm embryos, however, the same biochemical circuit produces transient and seemingly-stochastic focal "pulses" of Rho activity [48, 53, 54], which move slowly through the cortex before being extinguished. As we later show, the behavior in worms is not readily reproducible using classical Turing-type models [55], making it unclear how differences in patterns could arise from manipulation of the biochemical circuit.

Here we show that quantitative differences in Rho activity can be explained by accounting for variations in actin network architecture across model systems. Specifically, we implement a "hybrid" model which couples Turing-type continuum dynamics of Rho to a discrete actin network undergoing turnover. This model not only reproduces all of the experimentally-observed phenotypes, but also infers parameters from data that are consistent with available independent measurements. To gain conceptual insights, we extract the essential features of the hybrid model and express them within an improved continuum model, which reveals microscopic variation in network heterogeneity and stochasticity as a key "design principle" for biological control of pattern variation. Our overall approach integrating model development, data-driven inference, and mechanistic insight has the potential to be broadly applicable to other systems which feature structural diversity [56–59].

1 Variation in spatiotemporal Rho dynamics from conserved activator-inhibitor coupling with actin

1.1 Experimental data reveal context-dependent dynamics

Spatiotemporal dynamics of Rho activity can be read out in different systems by making time-lapse movies of fluorescently-tagged biosensors that selectively bind active Rho. To establish a framework for comparison of patterns across systems, we standardize a set of movies [20, 54] from starfish oocytes and *C. elegans* embryos by selecting a representative sample of the relevant dynamics. To remove boundary effects, we focus on a region in the embryo interior, then perform further filtering to remove noise (see Methods).

In starfish ooctyes, direct observations of a RhoA biosensor reveal a clear pattern of traveling waves [19, 20, 49]. In our representative example (Fig. 1B), these traveling waves are approximately synonymous with locally oscillatory dynamics, which have a period of roughly 60 s (see kymograph in Fig. 1B). By contrast, imaging the Rho biosensor in one-cell *C. elegans* embryos (Fig. 1C) yields a much lower signal-to-noise ratio, with significantly less regularity in the patterns of Rho excitations. Filtered images and kymographs (Fig. 1C) show irregular patches of excitation which seem to appear and disappear stochastically. These excitations have lifespans of about 25 s, during which they meander slowly in space, while maintaining sizes of about 10 μm^2.

1.2 Actin assembly dynamics modulate Rho activity

Simple activator-inhibitor models predict the traveling waves of Rho excitation observed in starfish oocytes [18–20, 49], but not the pulses observed in *C. elegans*. One notable difference between the systems is that there is significantly more actin network heterogeneity in *C. elegans* embryos [48] than in starfish and frog oocytes [19]. Previous *in silico* studies [55, 60, 61] suggest that this heterogeneity could contribute to a wider range of model behaviors. Similarly, previous experimental perturbations showed that modifying actin assembly dynamics could induce changes in patterns of Rho activity [54, 62–64]. We thus hypothesize that the actin network architecture and assembly dynamics are responsible for the observed differences in patterns.

As a first step toward validating this hypothesis, we re-examine previously-reported [54] spatiotemporal Rho dynamics in *C. elegans* embryos depleted of profilin (which promotes filament elongation [34, 65–67]) or formin (which promotes filament nucleation and elongation [35, 65, 66]). To avoid the confounding effects of contractility, these experiments were performed in embryos depleted of myosin II, which manifest the essential features of Rho dynamics observed in wildtype cells [54]. Compared to control embryos depleted of myosin alone, embryos co-depleted of myosin II and either formin or profilin exhibit larger Rho excitations (Fig. S2–S3). In filtered data, these excitations tend to recur in similar locations more frequently than in controls (Fig. 1D and E; see also [54, Fig. 8]). These data indicate that variation in actin network architecture and filament assembly dynamics tune the duration and spatial spread of Rho excitations [54].

1.3 Statistics for model inference

Given the inherent noise in the Rho activity data, the different systems can only be quantitatively compared statistically. Following previous work [19, 20], we use the cross correlation function

$$R\left(\rho, f; \Delta r, \Delta t\right) = \frac{1}{Z} \sum_{j,k} \rho(r_j, t_k) f(r_j + \Delta r, t_k + \Delta t), \tag{1}$$

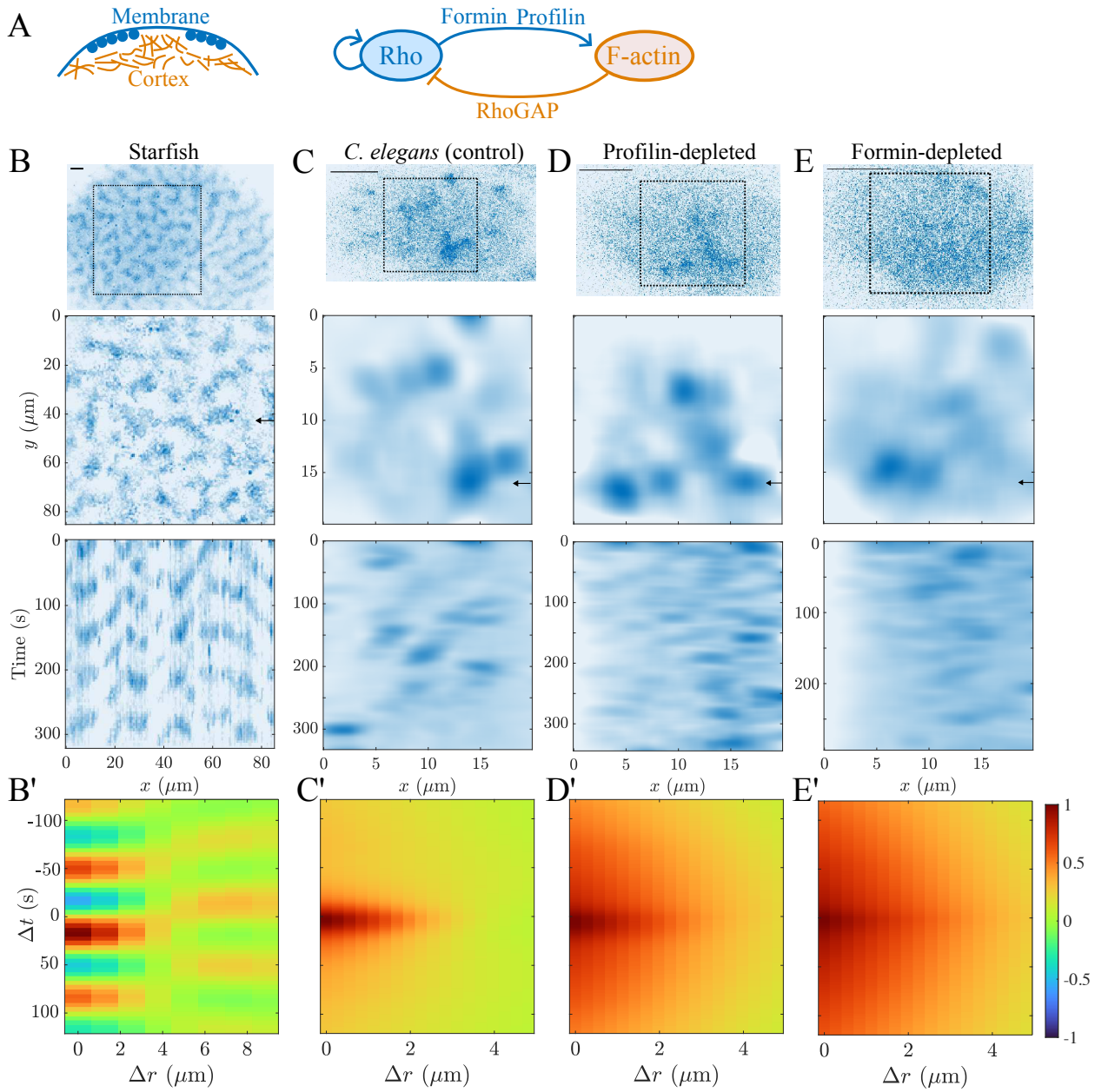

Figure 1: Activator-inhibitor coupling of Rho and actin generates diverse patterns of RhoA *in vivo*. (A) Rho and filamentous actin form an activator-inhibitor system at the cell cortex, with membrane-bound Rho assembling cortical actin filaments through its effectors (including formin and profilin), and actin filaments inhibiting Rho through RhoGAP. We abstract these dynamics down to two species: active Rho and F-actin (which we do not distinguish from RhoGAP). (B–E) Rho dynamics in (B) starfish [20, Fig. 1C] and (C–E) *C. elegans* embryos [(C) myosin(RNAi), (D) myosin+profilin(RNAi), and (E) myosin+formin(RNAi) [54]]. Top panels: raw data, scale bars = 10 μm. Middle panels: extracting a square region and filtering the result to identify excitations. Bottom panels: kymographs over the indicated y-slice (arrows in the middle panels). (B'–E') Cross correlation (1) between Rho and actin for each data set in (B–E).

between active Rho (ρ; the Rho biosensor) and F-actin (f; the RhoGAP/LifeAct signal) at a distance Δr away and time Δt later, where the normalization constant is chosen so that $\max(R) = 1$.

The cross correlation function puts the contrast between the starfish and *C. elegans* data in sharp relief (Fig. 1B' and C'): whereas the starfish cross correlation function is oscillatory in space and time in accordance with locally-oscillatory traveling waves, the *C. elegans* cross correlation function is positive almost everywhere, with a maximum at $(\Delta t, \Delta r) = (0, 0)$ that decays on length (2 μm) and time (25 s) scales corresponding to the typical size and lifetime of an excitation region. The cross correlation functions for the profilin- and formin-depleted embryos are broader in space and time (Fig. 1D' and E'), consistent with the larger and longer-lived excitations (Fig. S2–S3) in those systems.

2 Discrete-continuum model to infer actin assembly dynamics from experimental data

We now introduce a model that can reproduce the statistics of the experimental data, infer biologically-plausible parameter values, and suggest a mechanism for how actin architecture tunes Rho dynamics.

2.1 Coupling discrete actin assembly with continuum Rho dynamics

Let us first consider a classical activator-inhibitor model for the coupling between Rho and F-actin [68]. Letting ρ be the Rho concentration and f be the F-actin concentration, we set [48]

$$\partial_t \rho = D_\rho \nabla^2 \rho + k_\mathrm{b} + k_\mathrm{ac} \left(\frac{\rho^3}{\rho^3 + K_\mathrm{sat}} \right) - \left(k_\mathrm{inac}^{(0)} + k_\mathrm{inh} f \right) \rho \tag{2a}$$

$$\partial_t f = D_f \nabla^2 f + q_\mathrm{nuc} - k_\mathrm{diss}^{(\mathrm{act})} f. \tag{2b}$$

The Rho reaction-diffusion equation accounts for basal activation (k_b), auto-catalytic Rho activation (through the cubic Hill function), as well as enhanced inactivation of Rho by F-actin ($k_\mathrm{inh} f$). The F-actin equation captures actin filament assembly dynamics via the combination of local nucleation, isotropic diffusion, and local disassembly. Actin nucleation is enhanced in regions of higher Rho activity via the relationship

$$q_\mathrm{nuc}(\boldsymbol{x}) = q_b + q_\rho \rho(\boldsymbol{x})^2, \tag{2c}$$

and the isotropic diffusion term $D_f \nabla^2 f$ represents effective transport of F-actin due to elongation.

To represent a heterogeneous F-actin network with anisotropic growth, we replace the continuum description of actin dynamics (2b) with a discrete description in which individual filaments undergo nucleation, elongation and disassembly with kinetics similar to those observed in *C. elegans* embryos [67]. We assume that filaments nucleate stochastically with random orientation at discrete points in space, using the same rate (2c) as in the continuum model. Once nucleated, a filament polymerizes at the barbed end with rate ν_p to a maximum length ℓ_max, where it remains for time T_fil, after which it depolymerizes from the pointed end with rate ν_p (Fig. 2A). This discrete description captures essential features that do not appear in the continuum description, particularly stochastic nucleation and directional transport that arises through assembly and disassembly of individual filaments. In this model, the basal Rho inactivation rate $k_\mathrm{inac}^{(0)}$ combines the effects of basal GAP activity and homogeneous inhibition by an implicit background actin network, while the inhibition enhancement $k_\mathrm{inh} f(\boldsymbol{x})$ reflects the (heterogeneous) contribution of the explicit actin filaments.

2.2 Parameter estimation and inference

In the experimental systems that we examine, Rho dynamics are characterized by transitions between high and low activity states. To ensure that our model captures these dynamics, we choose the parameters in (2a) such that local Rho activity levels are close to a bifurcation (in the parameter $k_{\text{inac}} = k_{\text{inac}}^{(0)} + k_{\text{inh}} f$). As shown in Fig. S4, the dynamics of Rho fall into three categories as a function of k_{inac}. For low k_{inac}, there is a single steady state with high Rho concentration. For high k_{inac}, there is a single steady state with low Rho concentration. At intermediate k_{inac}, the Rho concentration is bistable.

Based on the bifurcation diagram, there are two plausible choices for $k_{\text{inac}}^{(0)}$, which sets the local behavior of Rho in the absence of F-actin. For small $k_{\text{inac}}^{(0)}$, any void in the actin network automatically initiates a pulse of Rho. For intermediate $k_{\text{inac}}^{(0)}$, Rho is bistable in the absence of F-actin; excitations do not initiate *de novo*, but spread from neighboring regions by diffusion. As we show in the SI (Section S2.4 and Fig. S6), the small $k_{\text{inac}}^{(0)}$ regime yields a negative cross-correlation between Rho and F-actin at $(\Delta r, \Delta t) = (0, 0)$, as low actin concentration is always correlated with high Rho concentration. This correlation pattern is inconsistent with the experimental data (Fig. 1), which leads us to choose an intermediate $k_{\text{inac}}^{(0)}$ where excitations spread by diffusion (with diffusivity $D_\rho = 0.1\ \mu\text{m}^2/\text{s}$ taken from experimental measurements [69]). Since only the product $k_{\text{inh}} f$ appears in (2a), we also fix k_{inh} to make f unique. This reduces the unknowns to the five F-actin assembly parameters: q_b, q_ρ, ν_p, T_{fil}, and $\ell_{\max}$ (Fig. 2A), which we vary to explore how emergent behaviors depend on local F-actin assembly dynamics.

To estimate the parameters from data, we define a posterior distribution $\Pi(\boldsymbol{x}|\boldsymbol{d})$ that gives the probability of observing the parameters $\boldsymbol{x}$ for each data set $\boldsymbol{d}$. This distribution can be sampled by choosing parameter set $\boldsymbol{x}$, running simulations to obtain simulated data, and computing the error in cross correlation (for all conditions) and excitation sizes (for *C. elegans* embryos only). See Methods for a more formal description of our inference procedure.

2.3 Discrete/continuum model reproduces Rho dynamics across model systems

We first ask whether the model can reproduce the variations in experimental data by tuning F-actin assembly dynamics. To this end, we obtain 5×10^5 independent samples of the model (simply by sampling uniformly within a bounded space, see Table S1), extract the parameter set with maximum posterior density for each data set, and visualize the model output in Fig. 2B.

Snapshots and kymographs reveal a strong resemblance to the experimental data (Fig. 1B). For the starfish data, the best fit simulations reproduce classical traveling waves, and the actin filaments are homogeneously distributed, with small lengths rendering their orientations superfluous. By contrast, best-fit simulations for *C. elegans* control embryos show actin filaments with lengths of a few microns, which create substantial heterogeneities in inhibitor dynamics. Snapshots and kymographs show how excitations escape through voids in the actin network, setting up a steady state of small, meandering patches of excitation which extinguish stochastically. In simulations that best match profilin- and formin-depleted embryos, these excitations grow in size, and cross correlations become broader in space and time. For simulations that best-match profilin-depleted embryos, this occurs because filaments are shorter, which confines the spread of inhibition, allowing excitations to spread until they run into filaments nucleated independently of Rho. For simulations that best-fit formin-depleted embryos, filaments are long and assemble rapidly from excitations. These long filaments give the most heterogeneous architecture, with large gaps through which excitations spread.

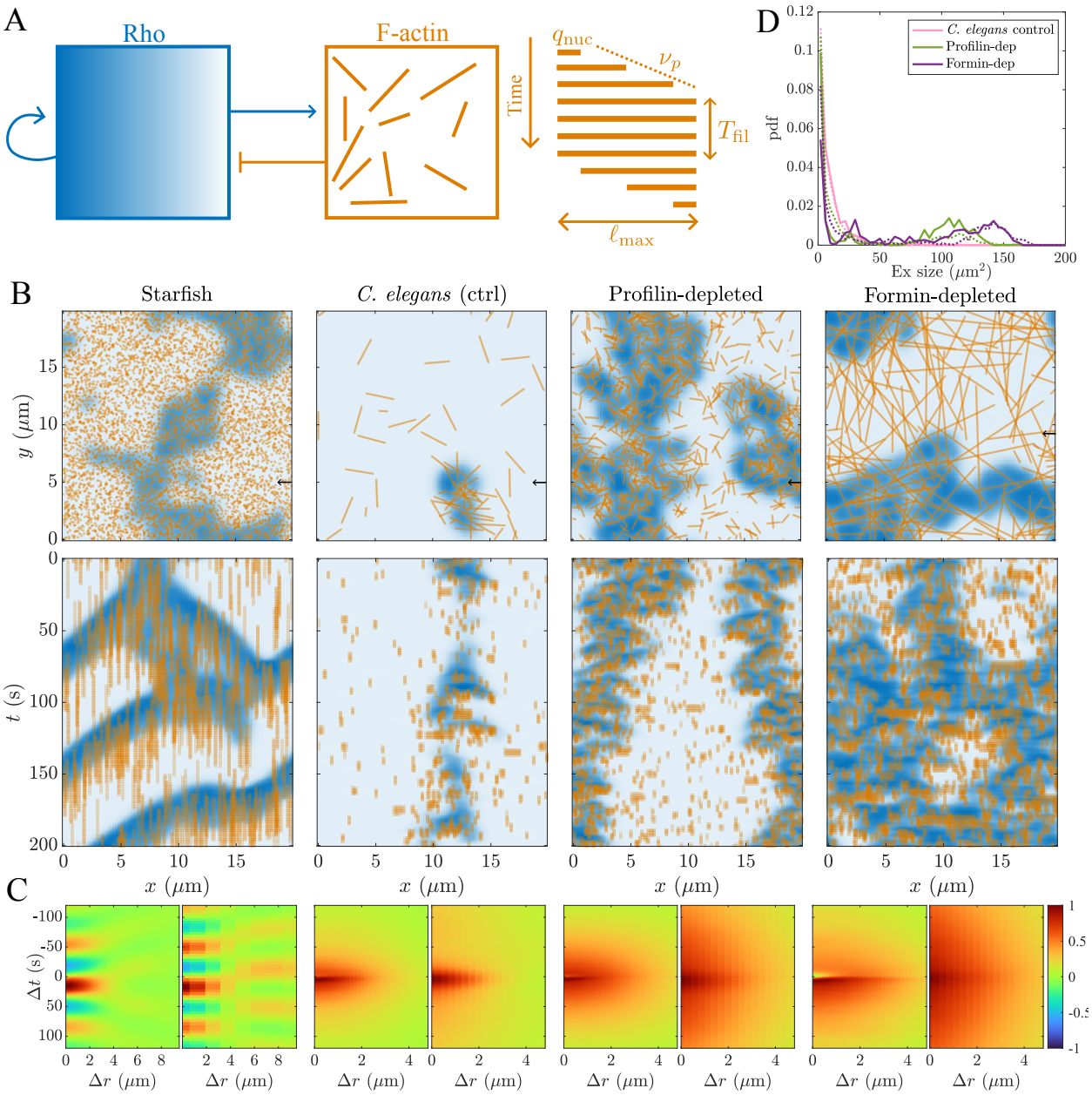

Figure 2: Hybrid discrete/continuum model reproduces experimental data across a variety of model systems and experimental conditions. (A) Model schematic. A continuum model of Rho is connected to a discrete actin network through activator-inhibitor coupling. Each discrete actin filament goes through the lifetime cycle shown at right: nucleation (rate given by (2c)), assembly (speed ν_p) to a fixed length ($\ell_{\rm max}$), a fixed time ($T_{\rm fil}$) spent at that length, and disassembly from the "older" end (speed ν_p). (B) Still images (at $t = 0$) and kymographs (along the indicated slices) for representative best-fit parameter sets for each experimental condition. (C) Cross correlations in the hybrid model (averaged over two simulations) compared to their experimental counterparts (right). (D) Excitation size distributions in the *C. elegans* parameter sets, compared to experimental data (dotted lines).

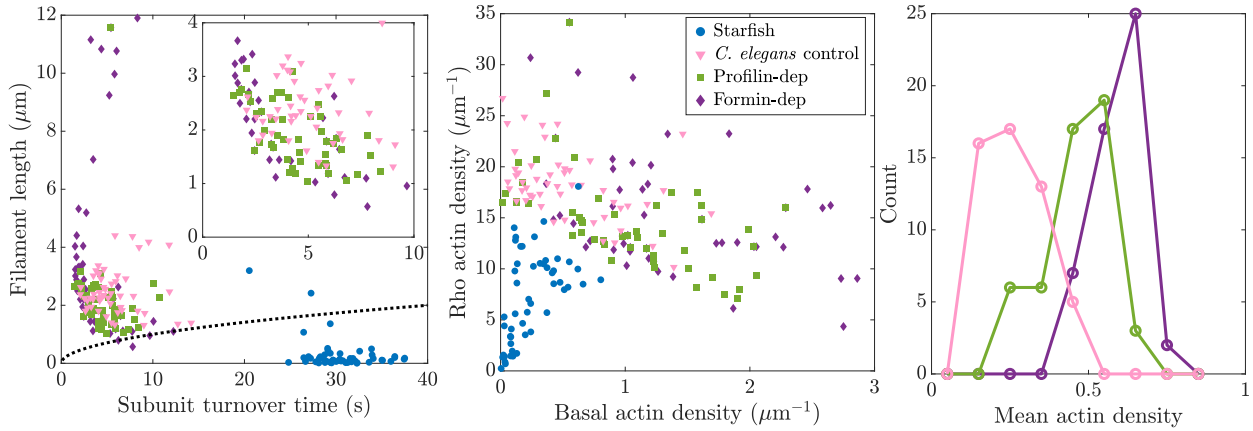

Figure 3: Hybrid model (constrained on cross correlations and excitation sizes) successfully infers actin kinetics in starfish and control *C. elegans* embryos, but misses key features of formin and profilin depletion. We show a series of statistics for the 50 (out of 5×10^5) highest-likelihood parameter sets in starfish (blue), and control (pink), profilin-depleted (green), and formin-depleted (purple) *C. elegans*. (Left) The subunit turnover time $T_{\text{sub}} = (T_{\text{fil}} + \ell_{\text{max}}/\nu_p)$ versus filament length ℓ_{max}. The dotted line shows the intrinsic Rho lengthscale $\ell_\rho(T_{\text{sub}}) = \sqrt{D_\rho T_{\text{sub}}}$, and the inset zooms in on the bottom left corner. (Middle) The density of actin from basal versus Rho-mediated nucleation. (Right) Distribution of mean actin densities (average number of filaments per grid cell) across the fifty most likely simulations.

2.4 Transforming inferred parameters into observables for model validation

To gain a mechanistic understanding of what drives phenotypic variation, we examine the parameter distributions obtained from the model. If the parameter distributions are in agreement with those measured (or anticipated) experimentally, then the model is likely learning the relevant dynamics. Otherwise, more information may be required to constrain model predictions.

To facilitate model validation, we transform the five F-actin assembly parameters into four observables that either have been measured experimentally or could be in the future. The first quantity is the turnover time of a monomer or subunit within a filament

$$T_{\text{sub}} = T_{\text{fil}} + \ell_{\text{max}}/\nu_p, \tag{3}$$

which can be measured by single-particle tracking of actin monomers bound to the cortex [36,48,69]. A second observable is the length of an actin filament ℓ_{max}, which can be measured by tracking single formin molecules as they polymerize F-actin at the barbed end (and multiplying the polymerization speed by the lifetime) [70]. The filament length ℓ_{max} quantifies the lengthscale of inhibition, which competes with the Rho diffusion lengthscale $\ell_\rho = \sqrt{D_\rho T_{\text{sub}}}$ over the lifetime of an actin subunit.

The two other observables convert the basal and Rho-mediated nucleation rates into a density (length of filamentous actin per square length of domain) of basal and Rho-mediated actin filaments on the cortex. Using an effective filament turnover rate,

$$k_{\text{diss}}^{(\text{act})} = \left(2\frac{\ell_{\text{max}}}{\nu_p} + T_{\text{fil}}\right)^{-1} \tag{4}$$

the total number density of basal and Rho-mediated filaments is given roughly by $N_b = q_b/k_{\text{diss}}^{(\text{act})}$ and $N_\rho = q_\rho \rho_{\text{max}}^2/k_{\text{diss}}^{(\text{act})}$, where ρ_{max} is the largest steady-state Rho concentration. In turn, the total length of basal/Rho-mediated actin per domain area is $L_{b/\rho} = \ell_{\text{max}} N_{b/\rho}$. These quantities

could be measured experimentally by computing the actin filament density in areas of high and low Rho activity, then solving a 2×2 system of equations to obtain L_b and L_ρ.

Figure 3 shows the observables for the fifty parameter sets with maximum posterior density in each experimental condition. Comparing likely parameters for starfish and control *C. elegans* embryos (blue and pink symbols), reveals a sharp difference in the rate of actin filament turnover and heterogeneity. The curve $\ell_p = \sqrt{D_\rho T_{\text{sub}}}$ (dotted black) demarcates the boundary above which the spread of inhibition exceeds the spread of excitation. Parameters for starfish fall below this line, indicating that actin dynamics lag Rho dynamics, while parameters for *C. elegans* fall above it, indicating that actin dynamics control the spread of Rho. For starfish parameters, subunit turnover times cluster around 30 s, while for control *C. elegans* the lifetimes are about 5–15 s (left panel of Fig. 3). Remarkably, the inferred mean turnover times agree with independent experimental measurements of 40 s [71, Fig. 5F] and 9 s [36, 69]. The inferred filament lengths of a few microns are also similar to those measured in control *C. elegans* embryos (up to 6 μm [70]). Thus, our model reveals that the excitation dynamics (technically, the summary statistics of cross correlation and excitation size) in control *C. elegans* embryos actually *imply* the microscopic F-actin dynamics (at least, the ones that have been measured to date).

Previous work [36, 54, 67] showed that embryos depleted of profilin have longer turnover times and shorter filament lengths, while embryos depleted of either profilin or formin have significantly less overall actin. Our parameter inference matches some of these observations but not others; parameter sets for profilin depletion typically have shorter filament lengths (see green squares in Fig. 3), but these parameter sets also display shorter subunit turnover times than controls. Significantly, both the profilin- and formin-depleted embryo simulations have higher actin densities than controls (right panel of Fig. 3), in disagreement with experimental observations.

2.5 Correcting actin dynamics with prior knowledge

The failure of the model to reproduce experimentally-relevant actin densities means that those observations are not embedded in the cross correlation and excitation sizes (which is the only information the model has). In fact, because the cross correlation between Rho and actin is positive everywhere in *C. elegans* embryos, data sets with the most Rho activity (formin-depletion) have the highest inferred actin concentration. Thus, we must incorporate what we already know about actin dynamics, which we do by modifying our inference procedure to include a penalty on unphysical parameter sets (see (5e) in Methods). In particular, we bias parameter sets to increase the amount of actin in simulations of control *C. elegans* embryos and decrease the amount of actin in simulations of formin- and profilin- depleted embryos. In simulations of profilin-depleted embryos, we also select for parameter sets with subunit turnover times T_{sub} that are roughly double those in controls.

Repeating our search through parameter space with the constrained F-actin dynamics, the best-fit parameter sets in control embryos now have more F-actin than profilin- and formin-depleted ones (Fig. 4A). Examining the best-fit simulations once again, control embryos have more actin filaments in regions of low Rho activity, which prevents much spread of excitations relative to the other conditions. The profilin-depleted phenotype is roughly unchanged, as filaments are significantly shorter than controls and excitations are larger (they spread instead of shrink). Penalizing the amount of F-actin completely removes the long filament phenotype previously observed for formin depletion; instead, we obtain excitations which readily grow and move through the regions lacking F-actin. As might be expected, the summary statistics (cross correlations and excitation sizes) do not line up as well in the simulations constrained on F-actin density. They do, however, reproduce the general trends of the data: excitation sizes are larger in formin and profilin depleted embryos, and cross correlations are wider in space (the spread in time appears roughly the same across all

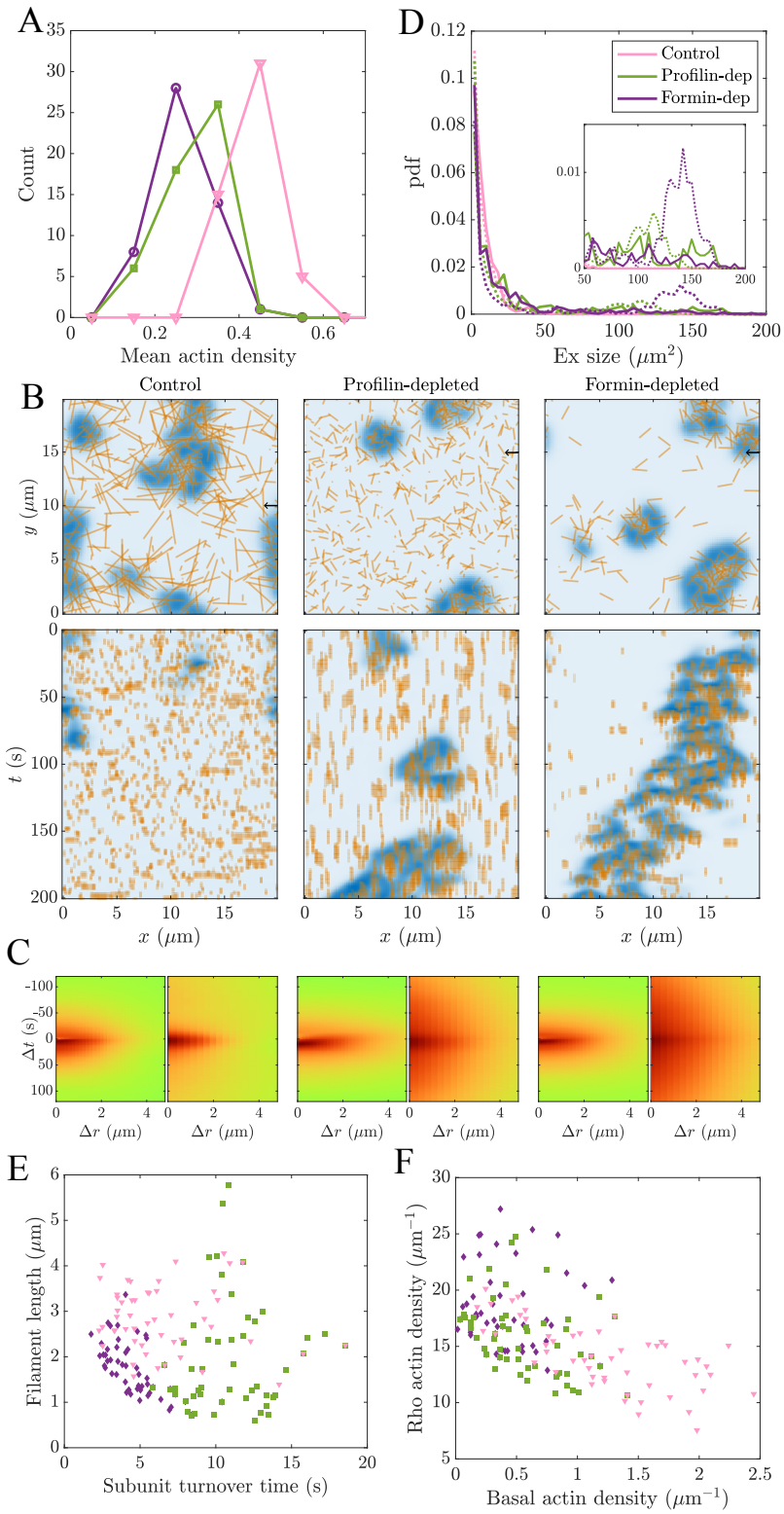

Figure 4: Constraining actin density and kinetics yields best-fit simulations that align with experimental observations. (A) F-actin densities for fifty best-fit parameter sets obtained when enforcing the ordering of mean F-actin density (see (5e)). (B) Most likely parameter set for each data set (starfish are unchanged from Fig. 2 and omitted). Top plot shows snapshot at $t = 0$, bottom plot shows kymographs over the indicated slices. (C) Cross correlations and (D) excitation size distributions for the simulations shown in (B); inset magnifies sizes in range $[50, 200]$. (E,F) Fifty most likely parameter sets (highest posterior densities), using the same measurables as Fig. 3.

simulations).

2.6 Prior-informed simulations constrain inferred parameters into clusters

The constrained F-actin dynamics allow for a biologically-realistic assessment of what parameters might be responsible for changes in excitation patterns. Among the worm embryos, a clear trend emerges in parameter space when moving between mutants. In the fifty parameter sets with highest posterior density (Fig. 4E,F), control embryos retain the characteristic turnover rate of 5–15 s. The long-filament phenotype is removed from the formin-depleted parameter sets (because the F-actin density is too high), and filaments are shorter with a slightly faster turnover rate than controls (Fig. 4E). Profilin-depleted parameter sets typically have shorter filament lengths than controls as well (green squares in Fig. 4E).

Perhaps the most interesting effect of incorporating the prior density is the clear trend that emerges in the basal versus Rho-mediated F-actin density plot (Fig. 4F). Control embryos have high basal F-actin densities and low Rho-mediated F-actin densities, while profilin- and formin-depleted embryos have low basal F-actin densities and high Rho-mediated actin densities. This comparison suggests that reducing the amount of basal actin and increasing the amount of Rho-mediated F-actin favors larger excitations.

3 Using an augmented continuum model to interpret the hybrid model

The hybrid model's ability to fit multiple data sets and produce parameter estimates consistent with available measurements suggests that it captures the relevant dynamics of the Rho/F-actin system. At the same time, the model's relatively dramatic departure from the classical continuum model (2) makes it difficult to determine the precise feature(s) responsible for its adaptability. In this section, we use the trends revealed by the hybrid model to obtain mechanistic insight via improved continuum modeling.

3.1 Simple continuum models easily fit starfish but not *C. elegans* data

We begin by establishing a baseline continuum model with F-actin turnover and diffusion rates consistent with values obtained from the hybrid model (see Section S3.1 and Table S3). To mimic the starfish parameter sets, we simulate the classical model (2) with low F-actin turnover rate and diffusivity, observing traveling waves with oscillatory cross correlation (Fig. 5A). In an attempt to transform these dynamics into transient pulses, we increase the F-actin turnover and diffusion rates, but find that standing patterns of excitation result (Fig. 5B). This behavior is consistent with that of previous continuum models [11, 18, 59] and indicates that additional features of the hybrid model are necessary to match the *C. elegans* data.

3.2 Spatial heterogeneities explain the lifetime and size of excitations

To understand what parts of the hybrid model enable it to capture both traveling waves and transient pulses, we decompose the stochasticity of the hybrid model into two sources of noise: the random spatial nucleation of actin filaments, and the random orientation with which they polymerize. To account for spatial stochasticity, we partition our periodic domain into irregularly-shaped regions of mean size A and define the nucleation rates (q_b and q_ρ) to be piecewise constant on each region, distributed randomly on $[0, 2q_b]$ and $[0, 2q_\rho]$, respectively (a one-dimensional slice

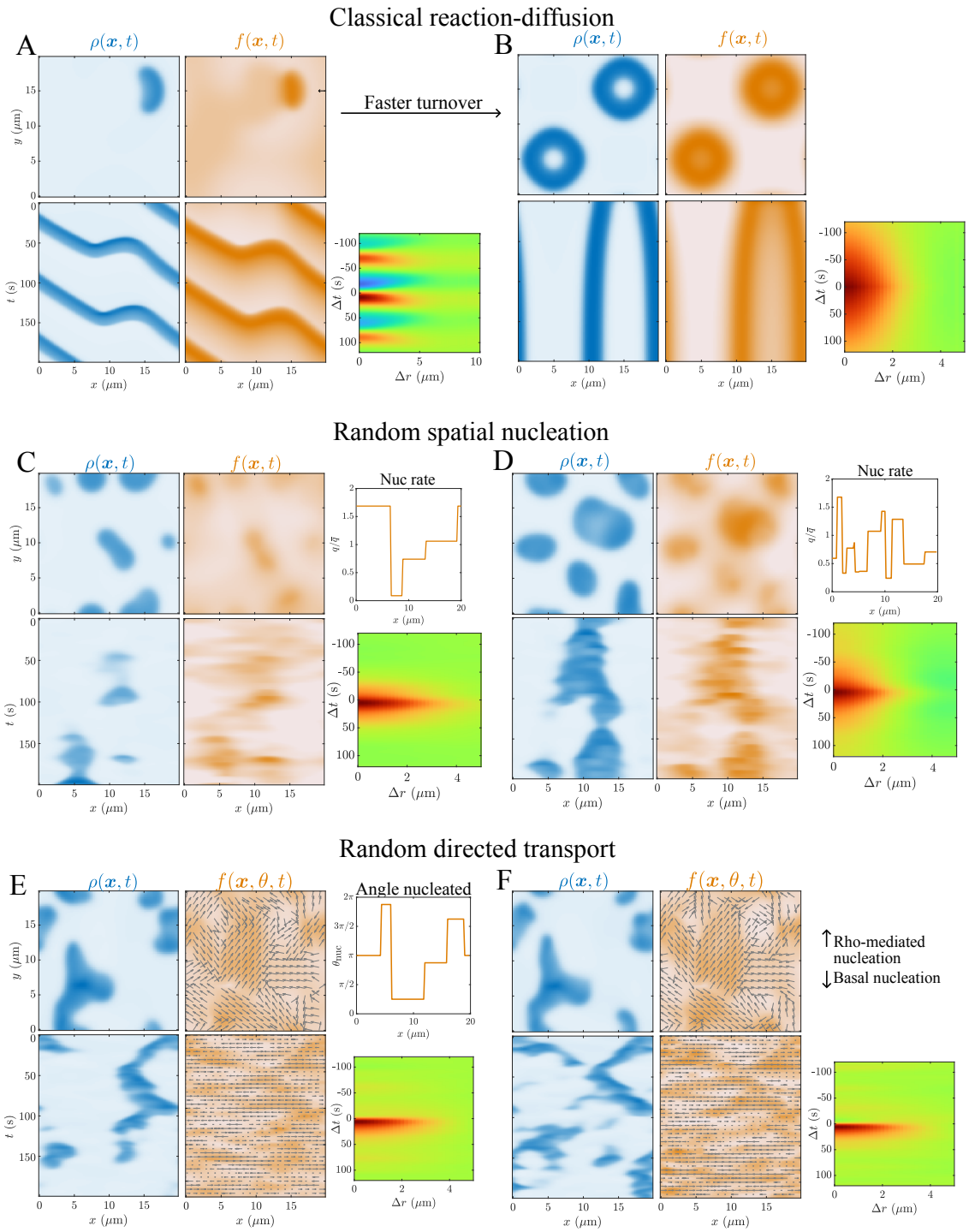

Figure 5: Accounting for spatial and orientational randomness in continuum models interprets the output of the hybrid model. (A–B) Simulations of the continuum model (2) with isotropic diffusion. (A) A parameter set with F-actin turnover $1/k_{\text{diss}}^{(\text{act})} = 30$ s yields traveling waves reminiscent of the starfish data. (B) Decreasing the F-actin turnover time to 8 s yields standing patterns in the continuum model. (C–D) The same model with the same parameters as (B), but with random rates of nucleation which turn over every $1/k_{\text{diss}}^{(\text{act})}$ s. In (C), the lengthscale of random nucleation is $\sim$4 μm, while in (D) it is halved to 2 μm (these simulations interpret the small filament phenotype). (E–F) Altering the model so that F-actin is transported advectively (via treadmilling) instead of by diffusion. Dynamics are governed by (6), and arrows show the most likely orientation of actin filaments. In (F), the parameters of (E) are modified to reduce basal nucleation and increase Rho-mediated nucleation.

of these rates is shown in Fig. 5C). Using an area of $A = 16\ \mu\text{m}^2$ for the region size (corresponding to an anisotropic lengthscale of 4 μm, which is the scale of the inferred filament length in the hybrid model), the excitations become transient (Fig. 5C), with fast F-actin turnover prompting the appearance and disappearance of Rho pulses [55], and a sharpening of the cross correlation to become similar to control embryos (Fig. 5C).

Interestingly, halving the lengthscale of spatial randomness (to 2 μm or $A = 4\ \mu\text{m}^2$) gives *larger*, more persistent patches, and a broader cross correlation (Fig. 5D). Indeed, to destabilize the excitations (Fig. 5B), the lengthscale of fluctuations in the nucleation rate must be larger than the lengthscale of the intrinsic standing patterns. This explains why shorter filament lengths were inferred in formin- and profilin-depleted embryos, where excitations are larger and more persistent. Notably, rapid diffusion of (isotropically-oriented) F-actin still keeps newly-formed pulses in these simulations from diffusing through space. Thus, the *spatial* randomness in the hybrid model can explain the transition from traveling waves to pulses with varied size, but cannot reproduce transport of pulses.

3.3 Orientational heterogeneities explain the spread of excitations

To understand the mobility of excitations in space, we extend the continuum model to account for transport via filament growth (instead of diffusion) in random directions. We maintain a constant nucleation rate, but endow the local F-actin density with an orientation θ (so that $f \equiv f(\boldsymbol{x}, \theta)$) and associated tangent vector $\boldsymbol{\tau} = (\cos\theta, \sin\theta)$. Directional advection (not isotropic diffusion) occurs in the $\boldsymbol{\tau}$ direction with speed $\nu_p = 1\ \mu\text{m/s}$ (modeling treadmilling, see (6) in Methods for equations) [61, 72–76]. Similar to the spatially random case, we partition the domain into regions which turn over every $1/k_{\text{diss}}^{(\text{act})} = 8$ s, and define a unique *angle* of nucleation on each region, keeping the total *rate* of nucleation constant across all of space (Fig. 5E shows a one-dimensional slice of the nucleated angle when $A = 16\ \mu\text{m}^2$). Introducing orientational noise in nucleation (Fig. 5E) shows how the directional growth of actin filaments allows for the spread of excitations. Because transport of F-actin occurs rapidly ($\nu_p = 1\ \mu\text{m/s}$), actin treadmilling always outpaces diffusion of Rho ($\nu_p t > \sqrt{D_\rho t}$ for $t > 0.1$ s), and the diffusion of Rho excitations can only occur in the direction *opposite* filament treadmilling (on the kymographs in Fig. 5E,F, there is no spread of Rho excitations in the direction of the pointed actin arrows). The spread of Rho into F-actin voids manifests itself in the cross correlation, which is more negative on $(\Delta r = 0, \Delta t < 0)$.

Recalling that the hybrid model predicted less basal F-actin and more Rho-mediated F-actin for profilin- and formin-depleted embryos, we modify our simulation by decreasing q_b and increasing q_ρ in the continuum nucleation rate (2c), keeping the random region size fixed at 16 μm^2 (Fig. 5F). Because there is less basal F-actin, excitations are more prone to spread, and they appear to move with faster speeds (compare the kymographs in Figs. 5E and F). Yet, the increase in Rho-mediated nucleation prevents the excitations from growing indefinitely, or from becoming traveling waves with negative cross correlations. Thus, the observation of spreading excitations (and their relative speeds) can be explained by accounting for the random orientation of actin filaments, in concert with a balance of basal and Rho-mediated F-actin assembly.

4 Discussion

In this paper, we used the activator-inhibitor interaction between active Rho and actin filaments at the cell cortex as a paradigm to understand how changes in microscopic parameters could lead to large-scale variations in self-organization. We presented data showing how a set of conserved

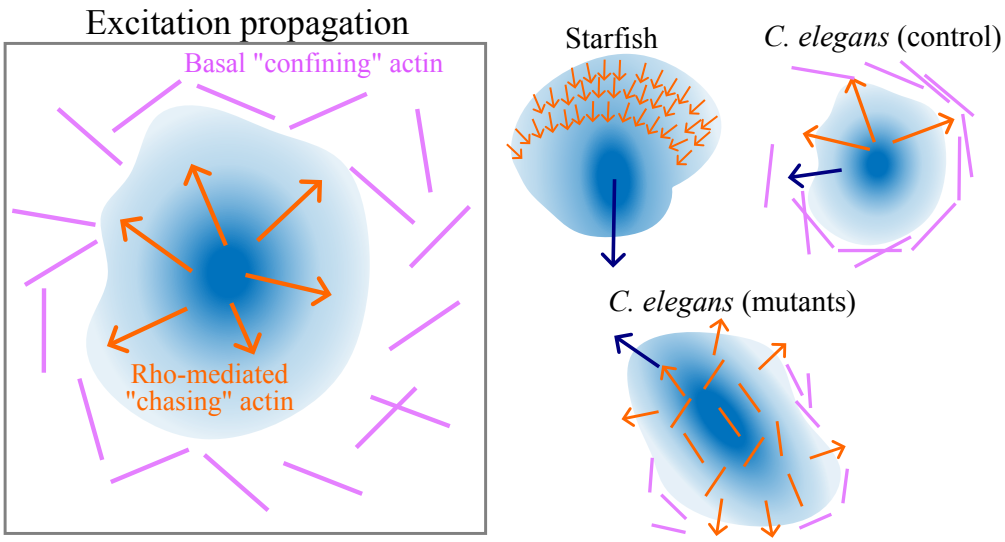

Figure 6: Schematic diagram demonstrating how basal and Rho-mediated actin confine and chase excitations, and how this process is adapted in starfish and *C. elegans* to produce pattern variation. In all cases, the active Rho wavefront spreads by diffusion, confined by "basal" F-actin (nucleated independent of Rho, purple) and chased by Rho-mediated assembly of F-actin (orange). In starfish embryos, low basal activity and slow F-actin elongation lead to traveling waves of Rho activity. *C. elegans* embryos have significantly higher rates of F-actin assembly, but more heterogeneous F-actin; this limits the size of excitations while allowing spread through network voids. In profilin- and formin-depleted embryos, filaments are shorter and basal F-actin assembly is reduced, reducing the spread of inhibition and leading to larger excitations.

biochemical interactions can give rise to traveling waves in starfish and frogs, and transient pulses in worms. Based on previous experiments [54, 71], we hypothesized that the differences between the two systems could come from the underlying F-actin dynamics. To test this, we introduced a hybrid model that coupled discrete actin filament dynamics to continuum dynamics of Rho. Our analysis of the model focused on two goals: first, to infer quantities which are hard to measure (microscopic parameters of actin dynamics) from those which are easy to measure (cell-scale concentration fields), and second, to understand how changes in the parameters governing F-actin assembly lead to the corresponding changes in observed excitation dynamics. While the experimental data [20, 54] and modeling techniques [48, 60, 68, 75–77] all existed previously, the novelty of our approach comes from the close interaction between the experiments and models. By extracting a set of summary statistics from the data, we formulated a posterior probability distribution, which we maximized to infer the parameter sets responsible for each phenotype.

We first asked the model to infer parameter sets using only the cross correlation function between Rho and F-actin and, for *C. elegans* embryos, the typical excitation sizes. In this case, the model predicted rates of F-actin turnover and filament lengthscales that agreed with previous measurements in starfish and *C. elegans* controls [36, 69, 71]. When fitting the data for formin- and profilin-depleted embryos, which have larger excitations and diffuse cross correlation profiles, the model initially inferred parameters inconsistent with qualitative expectations. Thus, in these embryos, cross correlation and excitation size alone do not supply sufficient information to infer the correct F-actin dynamics. To address this issue, we introduced a constraint on the amount of actin, under which the model inferred shorter filaments and less basal actin assembly in profilin- and formin-depleted embryos. This result provides a prediction for further model validation, which can be tested experimentally by obtaining more detailed measurements of filament length and density, in concert with reducing measurement noise in the data (Fig. 1(C–E)).

The combination of hybrid and continuum modeling provided a mechanistic picture of how F-actin assembly dynamics shape the spread of Rho activity *in vivo*. Rho acts as a spreading wavefront that is confined by basal F-actin (F-actin assembled independently of Rho) and chased by elongation of Rho-mediated filaments (Fig. 6). Starfish have homogeneous distributions of slowly elongating filaments, which assemble behind traveling wavefronts of Rho excitation. *C. elegans* embryos, by contrast, have actin filaments which elongate more rapidly, making the spread of inhibition faster than the spread of excitation. In classical continuum models of the Rho/F-actin circuit, faster spread of inhibition can only produce standing patterns, as actin filaments rapidly polymerize outward from excitations to cage them. However, our hybrid model reveals that in *C. elegans*, the F-actin network is sufficiently heterogeneous to leave gaps through which excitations can escape. These excitations spread until Rho-mediated F-actin catches up with them, or until they run into actin filaments nucleated independently of Rho. These are not traditional traveling waves; because the rapid assembly of F-actin still dominates in most directions, a positive cross correlation between Rho and F-actin results at all times. Our analysis suggests that the same mechanism operates in formin- and profilin-depleted embryos, with changes in filament length and the balance of basal and Rho-mediated F-actin assembly leading to larger excitations which spread more rapidly. Shorter filament lengths reduce the spread of inhibition and make actin more homogeneous, resulting in larger excitations and more diffuse cross correlations. Reduced basal actin allows excitations to spread faster, making the dynamics more wave-like, as was observed previously [54].

This work establishes our ability to infer parameters of microscopic actin assembly dynamics from cell-scale concentration data. This opens up an exciting future direction: using Rho and F-actin concentrations as probes to learn how various actin-binding proteins alter F-actin dynamics. By analyzing depleted versus control embryos, our model could predict how annilin, septin [63], or anterior PARs [78, 79] affect actin assembly dynamics through analysis of Rho excitation patterns and actin concentration fields. These accessory proteins are known or hypothesized to impact actin filament assembly, but understanding how they do so is often confounded by multiple downstream effects which lead to complex phenotypes. Our approach could isolate the effects of these proteins on Rho GTPase dynamics, which would ultimately give insights into how they affect fundamental processes such as cytokinesis and migration. Many of the observed phenotypes depend on myosin-mediated contractility [54, 80, 81], which requires straightforward (in the continuum setting [38, 49]) or more challenging (for discrete filaments [82, 83]) extensions to our methodology to incorporate. The interplay between biochemistry and contractility will open up a broader range of possible excitation patterns and principles for self organization [38, 39, 50, 51, 84, 85].

Our work also leads to new directions in mathematical analysis and computational science that go beyond the actin cytoskeleton. By using our discrete simulations to re-inform a continuum model, we demonstrated the importance of inhibitor heterogeneities—specifically spatial and orientational noise—in shaping the overall dynamics of activator-inhibitor systems. At this continuum level, a first-principles set of equations for anisotropic inhibition (obtained via homogenization theory [86, 87]) would significantly advance our understanding of self-organization in many biological systems. In the computational setting, applying our methodology to larger and more complicated biological systems will require methods that can efficiently sample high-dimensional parameter spaces. The first challenge here is to formulate a robust likelihood function for chaotic systems, optimizing summary statistics in the presence of chaotic trajectories [28, 88–91]. For sampling, methods that compute an "amortized" or approximate likelihood (potentially via machine learning) seem particularly promising because they avoid repeated calls to the high-fidelity forward model [27, 92–94]. Using these and other methods to leverage the large volumes of *in vivo* imaging data now available will enable us to deploy the approaches described here at scale.

Data availability

Code for simulations and data analysis is available at `https://github.com/omaxian/RhoActinRD`

Acknowledgments

All simulations were carried out on the RCC Midway research cluster at University of Chicago. OM was supported by the Yen and Chicago fellows program, and is now supported by a Spark Fellowship from the Physics Frontier Center for Living Systems (CLS) funded by the National Science Foundation (PHY-2317138); ARD and EM also acknowledge support from the CLS.

Methods

Data analysis

For the starfish data, we select a region in the embryo interior and perform difference subtraction to remove static Rho signal [20]. For the *C. elegans* data, we consider $N = 3$ embryos for each condition, cut out a 20 μm $\times$ 20 μm section in the embryo interior, then correct for photobleaching by adjusting the mean intensity of every frame to be equal to the global mean. We filter the data in space and time using a Savitzky-Golay filter with window size 50 pixels/frames (5 μm/30 s), and compute cross correlations on the filtered data (see Figs. S1–S2). To identify excitations in the filtered data, we set a threshold for excitations equal to $\rho_{\text{thres}} = \bar{\rho} + 0.1\,(\max(\rho) - \bar{\rho})$, where $\bar{\rho}$ is the mean Rho level, and the maximum is over all (filtered) pixels in space and time. We then use standard image processing algorithms (`bwconncomp` in Matlab) to identify connected regions of excitation and make a histogram of excitation sizes (see Figs. S2–S3).

Data-driven posterior estimation

Using Bayes' theorem, the posterior $\Pi(\boldsymbol{x}|\boldsymbol{d})$ can be related to the likelihood $\mathcal{L}(\boldsymbol{d}|\boldsymbol{x})$ and prior $\mathcal{P}(\boldsymbol{x})$ by

$$\Pi(\boldsymbol{x}|\boldsymbol{d}) \propto \mathcal{L}(\boldsymbol{d}|\boldsymbol{x})\mathcal{P}(\boldsymbol{x}) \rightarrow -\log \Pi = -\log \mathcal{L} - \log \mathcal{P} + C. \tag{5a}$$

The prior assigns low probability to unphysical parameter sets, while the likelihood function quantifies the errors in the summary statistics of cross correlation and excitation size:

$$-\log \mathcal{L}(\boldsymbol{x}) = \mathcal{E}_{\text{XCor}}(\boldsymbol{x}) + \mathcal{E}_{\text{Size}}(\boldsymbol{x}) \tag{5b}$$

$$\mathcal{E}_{\text{XCor}}(\boldsymbol{x}) = \frac{1}{\mathcal{E}_0} \sum_i \sum_j \left(R_{\rho f}^{\text{Sim}}(\Delta r_i, \Delta t_j; \boldsymbol{x}) - R_{\rho f}^{\text{Data}}\left(\Delta r_i, \Delta t_j\right) \right)^2 \tag{5c}$$

$$\mathcal{E}_{\text{Size}}(\boldsymbol{x}) = \frac{1}{\mathcal{S}_0} \sum_i \left(p_r^{\text{Sim}}(r_i) - p_r^{\text{Data}}(r_i) \right)^2 r_i. \tag{5d}$$

In (5c), $R_{\rho f}^{\text{Sim}}(\boldsymbol{x})$ and $R_{\rho f}^{\text{Data}}$ denote the simulated and experimental cross correlations, respectively, $\mathcal{E}_0$ is set so that $\mathcal{E}_{\text{XCor}} = 1$ when $R_{\rho f}^{\text{Sim}} = 0$, and the simulated cross correlation is resampled at the experimental data points by bilinear interpolation. Likewise, in (5d), $p_r^{\text{Sim/Data}}$ denotes the PDF of excitation sizes from simulations/data, and $\mathcal{S}_0$ is again set so that $\mathcal{E}_{\text{Size}} = 1$ when there are no excitations. The weight of r_i ensures that excitations are counted based on overall area and not absolute number; i.e., one excitation of size 200 μm^2 weighs the same as 200 excitations of size 1 μm^2. This gives a more faithful representation of errors in systems with large excitations (which are fewer in absolute number and therefore easier to discount without the weights). Finally, the $\mathcal{E}_{\text{Size}}$

term is omitted for the starfish data, as the cross-correlation function in that case is sufficiently long-ranged in space and time to convey all of the necessary information.

Prior densities

In initial parameter fitting (Fig. 2), we use a uniform prior on the parameter ranges given in Table S1. Subsequently (Fig. 4), we correct the posterior distribution using a prior on the actin density. Letting $\bar{f}$ be the mean actin density, we penalize a lack of actin in control embryos and a surplus of actin in depleted embryos by setting

$$-\log \mathcal{P}(\boldsymbol{x}) = \begin{cases} \left(\bar{f}/0.5 - 1\right)^2 \delta_{\bar{f}<0.5} & \text{Control embryos} \\ 2\left(T_{\text{sub}}/12 - 1\right)^2 \delta_{T_{\text{sub}}<12} + 2\left(\bar{f}/0.3 - 1\right)^2 \delta_{\bar{f}>0.3} & \text{Profilin-depleted} \\ 4\left(\bar{f}/0.3 - 1\right)^2 \delta_{\bar{f}>0.3} & \text{Formin-depleted} \end{cases} \tag{5e}$$

where δ_x is 1 if condition x is true and 0 otherwise. In addition to the density of actin, for profilin-depleted embryos we penalize subunit lifetimes shorter than 12 s, which is roughly double the average value for controls.

Re-informed continuum model

The continuum model that accounts for orientation (Fig. 5C) is defined by letting $f \equiv f(\boldsymbol{x}, \theta, t)$, where $\theta \in [0, 2\pi)$ is the local orientation of the filaments. Assuming directional advection (treadmilling) of the actin density along $\boldsymbol{\tau} = (\cos\theta, \sin\theta)$ with speed ν_p, the continuum equations (2) become (making the dependence on $\boldsymbol{x}$ and θ explicit for clarity)

$$\partial_t \rho(\boldsymbol{x}) = D_\rho \Delta\rho(\boldsymbol{x}) + k_{\text{b}} + k_{\text{ac}} \left(\frac{\rho(\boldsymbol{x})^3}{\rho(\boldsymbol{x})^3 + K_{\text{sat}}} \right) - \left(k_{\text{inac}}^{(0)} + k_{\text{inh}} \bar{f}(\boldsymbol{x}) \right) \rho(\boldsymbol{x}) \tag{6a}$$

$$\partial_t f(\boldsymbol{x}, \theta) = -\nabla_{\boldsymbol{x}} \cdot (\nu_p \boldsymbol{\tau}(\theta) f(\boldsymbol{x}, \theta)) + q_b(\boldsymbol{x}, \theta, t) + q_\rho(\boldsymbol{x}, \theta, t)\rho(\boldsymbol{x})^2 - k_{\text{diss}}^{(\text{act})} f(\boldsymbol{x}, \theta), \tag{6b}$$

where $\bar{f}(\boldsymbol{x}, t) = \int_0^{2\pi} f(\boldsymbol{x}, \theta, t)\, d\theta$ is the total amount of actin at each point.

Numerical methods

The continuum partial differential equations (2) and (6) are solved numerically using a combination of a psuedo-spectral method (for diffusion) with an implicit-explicit temporal discretization, where diffusion is handled implicitly (using the backward Euler method), and the reaction terms are handled explicitly (using forward Euler). In the directional transport equation (6), advection is handled explicitly via first-order upwinding. See [95, c. 1] for a description of these methods.

In the simulations with a discrete actin network, the actin dynamics occur in two steps: nucleation and polymerization. For nucleation, at each time step a filament nucleates in a grid cell centered at (x_i, y_j) if $r < q_{\text{nuc}}(x_i, y_j)\Delta x^2 \Delta t$, where $r \sim U(0, 1)$. Once nucleated, the filament is assigned a random tangent vector (normalized Gaussian) and random (uniform) start point in the box $(x_i, y_j) \pm (\Delta x, \Delta y)$. Polymerization and depolymerization thereafter are deterministic, where at each time step fibers grow/shrink by $\nu_p \Delta t$ length units, discretized into points $\boldsymbol{X}_j$ with spacing Δs (in the case when this results in a non-integer number of points added per time step, the remainder is handled stochastically such that the average growth/shrink rate is ν_p). The associated actin filament field $f(\boldsymbol{x})$ is defined by smearing the filaments with a Gaussian of width g_w,

$$f(\boldsymbol{x}) = F_0 \sum_{j=1}^{F} \exp\left(-\left\| \boldsymbol{x} - \boldsymbol{X}_j \right\|^2 / (2g_w^2) \right) \Delta s, \tag{7}$$

The constant F_0 (units of concentration per length) is chosen so that the actin field on the grid is 1 for a single filament. We implement fast Gaussian gridding [96, Sec. 3] to accelerate the sum (7).

References

[1] Jacob Halatek, Fridtjof Brauns, and Erwin Frey. Self-organization principles of intracellular pattern formation. *Philos. Trans. R. Soc. B*, 373(1747):20170107, 2018.

[2] Nathan W Goehring, Philipp Khuc Trong, Justin S Bois, Debanjan Chowdhury, Ernesto M Nicola, Anthony A Hyman, and Stephan W Grill. Polarization of PAR proteins by advective triggering of a pattern-forming system. *Science*, 334(6059):1137–1141, 2011.

[3] Peter Gross, K Vijay Kumar, Nathan W Goehring, Justin S Bois, Carsten Hoege, Frank Jülicher, and Stephan W Grill. Guiding self-organized pattern formation in cell polarity establishment. *Nat. Phys.*, 15(3):293–300, 2019.

[4] Charles F Lang and Edwin Munro. The PAR proteins: From molecular circuits to dynamic self-stabilizing cell polarity. *Development*, 144(19):3405–3416, 2017.

[5] John Cody Herron, Shiqiong Hu, Bei Liu, Takashi Watanabe, Klaus M. Hahn, and Timothy C. Elston. Spatial models of pattern formation during phagocytosis. *PLoS Comput. Biol*, 18(10):e1010092, October 2022.

[6] Sara A Wickström and Carien M Niessen. Cell adhesion and mechanics as drivers of tissue organization and differentiation: Local cues for large scale organization. *Curr. Opin. Cell Biol.*, 54:89–97, October 2018.

[7] Yoshiki Sasai. Cytosystems dynamics in self-organization of tissue architecture. *Nature*, 493(7432):318–326, January 2013.

[8] Adam Siepel, Gill Bejerano, Jakob S. Pedersen, Angie S. Hinrichs, Minmei Hou, Kate Rosenbloom, Hiram Clawson, John Spieth, LaDeana W. Hillier, Stephen Richards, George M. Weinstock, Richard K. Wilson, Richard A. Gibbs, W. James Kent, Webb Miller, and David Haussler. Evolutionarily conserved elements in vertebrate, insect, worm, and yeast genomes. *Genome Res.*, 15(8):1034–1050, August 2005.

[9] Ann M. Stock, Victoria L. Robinson, and Paul N. Goudreau. Two-component signal transduction. *Annu. Rev. Biochem.*, 69(1):183–215, June 2000.

[10] Alan Turing. The chemical basis of morphogenesis. *Phil. Trans. R. Soc. B*, 237:37–72, 1953.

[11] A. Gierer and H. Meinhardt. A theory of biological pattern formation. *Kybernetik*, 12(1):30–39, December 1972.

[12] Lee A. Segel and Julius L. Jackson. Dissipative structure: an explanation and an ecological example. *J. Theor. Biol.*, 37(3):545–559, December 1972.

[13] J.D. Murray. A pre-pattern formation mechanism for animal coat markings. *J. Theor. Biol.*, 88(1):161–199, January 1981.

[14] J.D. Murray. Parameter space for Turing instability in reaction diffusion mechanisms: a comparison of models. *J. Theor. Biol.*, 98(1):143–163, September 1982.

[15] Andrew L. Krause, Eamonn A. Gaffney, Philip K. Maini, and Václav Klika. Modern perspectives on near-equilibrium analysis of Turing systems. *Phil. Trans. R. Soc. A.*, 379(2213):20200268, December 2021.

[16] Andrew J. Bernoff. Spiral wave solutions for reaction-diffusion equations in a fast reaction/slow diffusion limit. *Physica D*, 53(1):125–150, October 1991.

[17] Arik Yochelis, Sven Flemming, and Carsten Beta. Versatile patterns in the actin cortex of motile cells: self-organized pulses can coexist with macropinocytic ring-shaped waves. *Phys. Rev. Lett.*, 129(8):088101, August 2022.

[18] William M. Bement, Andrew B. Goryachev, Ann L. Miller, and George Von Dassow. Patterning of the cell cortex by Rho GTPases. *Nat. Rev. Mol. Cell Biol.*, 25(4):290–308, April 2024.

[19] William M. Bement, Marcin Leda, Alison M. Moe, Angela M. Kita, Matthew E. Larson, Adriana E. Golding, Courtney Pfeuti, Kuan-Chung Su, Ann L. Miller, Andrew B. Goryachev, and George von Dassow. Activator–inhibitor coupling between Rho signalling and actin assembly makes the cell cortex an excitable medium. *Nat. Cell Biol.*, 17(11):1471–1483, November 2015.

[20] Ani Michaud, Marcin Leda, Zachary T Swider, Songeun Kim, Jiaye He, Jennifer Landino, Jenna R Valley, Jan Huisken, Andrew B Goryachev, George von Dassow, et al. A versatile cortical pattern-forming circuit based on Rho, F-actin, Ect2, and RGA-3/4. *J. Cell Biol.*, 221(8):e202203017, 2022.

[21] Cory M. Simon, Emily M. Vaughan, William M. Bement, and Leah Edelstein-Keshet. Pattern formation of Rho GTPases in single cell wound healing. *Mol. Biol. Cell*, 24(3):421–432, February 2013.

[22] Maria A. Kiskowski, Mark S. Alber, Gilberto L. Thomas, James A. Glazier, Natalie B. Bronstein, Jiayu Pu, and Stuart A. Newman. Interplay between activator–inhibitor coupling and cell-matrix adhesion in a cellular automaton model for chondrogenic patterning. *Dev. Biol.*, 271(2):372–387, July 2004.

[23] Zhanghan Wu, Maohan Su, Cheesan Tong, Min Wu, and Jian Liu. Membrane shape-mediated wave propagation of cortical protein dynamics. *Nat. Commun.*, 9(1):136, January 2018.

[24] Shigeru Kondo and Takashi Miura. Reaction-diffusion model as a framework for understanding biological pattern formation. *Science*, 329(5999):1616–1620, September 2010.

[25] Dominic Chomchai, Marcin Leda, Adriana Golding, George Von Dassow, William M. Bement, and Andrew B. Goryachev. Rho GTPase dynamics distinguish between models of cortical excitability. *Curr. Biol.*, page S096098222500137X, February 2025.

[26] David J. Warne, Ruth E. Baker, and Matthew J. Simpson. Using experimental data and information criteria to guide model selection for reaction–diffusion problems in mathematical biology. *Bull. Math. Biol.*, 81(6):1760–1804, June 2019.

[27] Antonio Matas-Gil and Robert G Endres. Unraveling biochemical spatial patterns: Machine learning approaches to the inverse problem of stationary Turing patterns. *iScience*, 27(6), 2024.

[28] Hidekazu Hishinuma, Hisako Takigawa-Imamura, and Takashi Miura. Data-driven discovery and parameter estimation of mathematical models in biological pattern formation. *PLoS Comput. Biol*, 21(1):e1012689, 2025.

[29] Yue Liu, Kevin Suh, Philip K. Maini, Daniel J. Cohen, and Ruth E. Baker. Parameter identifiability and model selection for partial differential equation models of cell invasion. *J. R. Soc. Interface.*, 21(212), March 2024.

[30] Andreas Buttenschön, Thomas Hillen, Alf Gerisch, and Kevin J. Painter. A space-jump derivation for non-local models of cell–cell adhesion and non-local chemotaxis. *J. Math. Biol.*, 76(1-2):429–456, January 2018.

[31] Matthew J Simpson, Ruth E Baker, Sean T Vittadello, and Oliver J Maclaren. Practical parameter identifiability for spatio-temporal models of cell invasion. *J. R. Soc. Interface*, 17:20200055, 2020.

[32] Michael A Dewar, Visakan Kadirkamanathan, Manfred Opper, and Guido Sanguinetti. Parameter estimation and inference for stochastic reaction-diffusion systems: application to morphogenesis in *D. Melanogaster*. *BMC Syst. Biol.*, 4(1), December 2010.

[33] David Schnoerr, Ramon Grima, and Guido Sanguinetti. Cox process representation and inference for stochastic reaction–diffusion processes. *Nat. Commun.*, 7(1), May 2016.

[34] Thomas D. Pollard, Laurent Blanchoin, and R. Dyche Mullins. Molecular mechanisms controlling actin filament dynamics in nonmuscle cells. *Annu. Rev. Biophys. Biomol. Struct.*, 29(1):545–576, June 2000.

[35] Thomas D Pollard. Regulation of actin filament assembly by Arp2/3 complex and formins. *Annu. Rev. Biophys. Biomol. Struct.*, 36:451–477, 2007.

[36] Younan Li and Edwin Munro. Filament-guided filament assembly provides structural memory of filament alignment during cytokinesis. *Dev. Cell*, 56(17):2486–2500, 2021.

[37] Anne-Cécile Reymann, Rajaa Boujemaa-Paterski, Jean-Louis Martiel, Christophe Guérin, Wenxiang Cao, Harvey F. Chin, Enrique M. De La Cruz, Manuel Théry, and Laurent Blanchoin. Actin network architecture can determine myosin motor activity. *Science*, 336(6086):1310–1314, June 2012.

[38] Michael F Staddon, Edwin M Munro, and Shiladitya Banerjee. Pulsatile contractions and pattern formation in excitable actomyosin cortex. *PLoS Comput. Biol*, 18(3):e1009981, 2022.

[39] Michael E. Werner, Dylan D. Ray, Coleman Breen, Michael F. Staddon, Florian Jug, Shiladitya Banerjee, and Amy Shaub Maddox. Mechanical and biochemical feedback combine to generate complex contractile oscillations in cytokinesis. *Curr. Biol.*, 34(14):3201–3214.e5, July 2024.

[40] Guillaume Salbreux, Guillaume Charras, and Ewa Paluch. Actin cortex mechanics and cellular morphogenesis. *Trends Cell Biol.*, 22(10):536–545, October 2012.

[41] Gijsje H Koenderink and Ewa K Paluch. Architecture shapes contractility in actomyosin networks. *Curr. Opin. Cell Biol.*, 50:79–85, February 2018.

[42] Priyamvada Chugh, Andrew G Clark, Matthew B Smith, Davide AD Cassani, Kai Dierkes, Anan Ragab, Philippe P Roux, Guillaume Charras, Guillaume Salbreux, and Ewa K Paluch. Actin cortex architecture regulates cell surface tension. *Nat. Cell Biol.*, 19(6):689–697, 2017.

[43] Alan Hall. Rho GTPases and the actin cytoskeleton. *Science*, 279(5350):509–514, 1998.

[44] Soon-Tuck Sit and Ed Manser. Rho GTPases and their role in organizing the actin cytoskeleton. *J. Cell Sci.*, 124(5):679–683, March 2011.

[45] Shawn N. Jordan and Julie C. Canman. Rho GTPases in animal cell cytokinesis: an occupation by the one percent. *Cytoskeleton*, 69(11):919–930, November 2012.

[46] Alisa Piekny, Michael Werner, and Michael Glotzer. Cytokinesis: welcome to the Rho zone. *Trends Cell Biol.*, 15(12):651–658, December 2005.

[47] Alan Hall and Catherine D. Nobes. Rho GTPases: Molecular switches that control the organization and dynamics of the actin cytoskeleton. *Phil. Trans. R. Soc. Lond. B*, 355(1399):965–970, July 2000.

[48] Jonathan B Michaux, François B Robin, William M McFadden, and Edwin M Munro. Excitable RhoA dynamics drive pulsed contractions in the early *C. elegans* embryo. *J. Cell Biol.*, 217(12):4230–4252, 2018.

[49] Sheng Chen, Daniel S. Seara, Ani Michaud, Songeun Kim, William M. Bement, and Michael P. Murrell. Energy partitioning in the cell cortex. *Nat. Phys.*, 20(11):1824–1832, November 2024.

[50] Manon C. Wigbers, Tzer Han Tan, Fridtjof Brauns, Jinghui Liu, S. Zachary Swartz, Erwin Frey, and Nikta Fakhri. A hierarchy of protein patterns robustly decodes cell shape information. *Nat. Phys.*, 17(5):578–584, May 2021.

[51] Jinghui Liu, Tom Burkart, Alexander Ziepke, John Reinhard, Yu-Chen Chao, Tzer Han Tan, S. Zachary Swartz, Erwin Frey, and Nikta Fakhri. Light-induced cortical excitability reveals programmable shape dynamics in starfish oocytes. *Nat. Phys.*, 21(5):846–855, May 2025.

[52] Junang Li, Chih-Wei Joshua Liu, Michal Szurek, and Nikta Fakhri. Measuring irreversibility from learned representations of biological patterns. *PRX Life*, 2(3), September 2024.

[53] Masatoshi Nishikawa, Sundar Ram Naganathan, Frank Jülicher, and Stephan W Grill. Controlling contractile instabilities in the actomyosin cortex. *eLife*, 6:e19595, January 2017.

[54] Baixue Yao, Seth Donoughe, Jonathan Michaux, and Edwin Munro. Modulating RhoA effectors induces transitions to oscillatory and more wavelike RhoA dynamics in *Caenorhabditis elegans* zygotes. *Mol. Biol. Cell*, 33(6):ar58, 2022.

[55] Inbal Hecht, David A. Kessler, and Herbert Levine. Transient Localized Patterns in Noise-Driven Reaction-Diffusion Systems. *Phys. Rev. Lett.*, 104(15):158301, April 2010.

[56] Melanie Graessl, Johannes Koch, Abram Calderon, Dominic Kamps, Soumya Banerjee, Tomáš Mazel, Nina Schulze, Jana Kathrin Jungkurth, Rutuja Patwardhan, Djamschid Solouk, Nico Hampe, Bernd Hoffmann, Leif Dehmelt, and Perihan Nalbant. An excitable Rho GTPase signaling network generates dynamic subcellular contraction patterns. *J. Cell Biol.*, 216(12):4271–4285, December 2017.

[57] Erik Bernitt, Hans-Günther Döbereiner, Nir S. Gov, and Arik Yochelis. Fronts and waves of actin polymerization in a bistability-based mechanism of circular dorsal ruffles. *Nat. Commun.*, 8(1):15863, June 2017.

[58] Günther Gerisch, Till Bretschneider, Annette Müller-Taubenberger, Evelyn Simmeth, Mary Ecke, Stefan Diez, and Kurt Anderson. Mobile actin clusters and traveling waves in cells recovering from actin depolymerization. *Biophys. J.*, 87(5):3493–3503, November 2004.

[59] Sayak Bhattacharya, Tatsat Banerjee, Yuchuan Miao, Huiwang Zhan, Peter N. Devreotes, and Pablo A. Iglesias. Traveling and standing waves mediate pattern formation in cellular protrusions. *Sci. Adv.*, 6(32):eaay7682, August 2020.

[60] Anders E. Carlsson. Dendritic actin filament nucleation causes traveling waves and patches. *Phys. Rev. Lett.*, 104(22):228102, June 2010.

[61] Stephen Whitelam, Till Bretschneider, and Nigel J. Burroughs. Transformation from spots to waves in a model of actin pattern formation. *Phys. Rev. Lett.*, 102(19):198103, May 2009.

[62] Luiza Stankevicins, Nicolas Ecker, Emmanuel Terriac, Paolo Maiuri, Rouven Schoppmeyer, Pablo Vargas, Ana-Maria Lennon-Duménil, Matthieu Piel, Bin Qu, Markus Hoth, Karsten Kruse, and Franziska Lautenschläger. Deterministic actin waves as generators of cell polarization cues. *Proc. Natl. Acad. Sci. U.S.A.*, 117(2):826–835, January 2020.

[63] Amy Shaub Maddox, Lindsay Lewellyn, Arshad Desai, and Karen Oegema. Anillin and the septins promote asymmetric ingression of the cytokinetic furrow. *Dev. Cell*, 12(5):827–835, May 2007.

[64] Sabrya C. Carim and Gilles R.X. Hickson. The Rho1 GTPase controls anillo-septin assembly to facilitate contractile ring closure during cytokinesis. *iScience*, 26(6):106903, June 2023.

[65] Aditya Paul and Thomas Pollard. The role of the FH1 domain and profilin in formin-mediated actin-filament elongation and nucleation. *Curr. Biol.*, 18(1):9–19, 2008.

[66] Aaron F. Severson, David L. Baillie, and Bruce Bowerman. A formin homology protein and a profilin are required for cytokinesis and Arp2/3-independent assembly of cortical microfilaments in *C. elegans*. *Curr. Biol.*, 12(24):2066–2075, December 2002.

[67] Elizabeth D White, Younan Li, Rachel Kadzik, Yuqing Qiu, Aaron R Dinner, and Edwin M Munro. Microscopic control of cortical flows in polarized *C. elegans* zygotes. *bioRxiv*, 2025.

[68] May Anne Mata, Meghan Dutot, Leah Edelstein-Keshet, and William R. Holmes. A model for intracellular actin waves explored by nonlinear local perturbation analysis. *J. Theor. Biol.*, 334:149–161, October 2013.

[69] François B Robin, William M McFadden, Baixue Yao, and Edwin M Munro. Single-molecule analysis of cell surface dynamics in *Caenorhabditis elegans* embryos. *Nat. Meth.*, 11(6):677–682, 2014.

[70] Vlad Costache, Serena Prigent Garcia, Camille N Plancke, Jing Li, Simon Begnaud, Shashi Kumar Suman, Anne-Cécile Reymann, Taeyoon Kim, and François B Robin. Rapid assembly of a polar network architecture drives efficient actomyosin contractility. *Cell Rep.*, 39(9), 2022.

[71] Brian M. Burkel, George Von Dassow, and William M. Bement. Versatile fluorescent probes for actin filaments based on the actin-binding domain of utrophin. *Cell Motil. Cytoskeleton*, 64(11):822–832, November 2007.

[72] David Saintillan and Michael J. Shelley. Orientational order and instabilities in suspensions of self-locomoting rods. *Phys. Rev. Lett.*, 99(5), July 2007.

[73] Donald L. Koch and Eric S. G. Shaqfeh. The instability of a dispersion of sedimenting spheroids. *J. Fluid Mech.*, 209:521–542, December 1989.

[74] David Saintillan and Michael J Shelley. Theory of active suspensions. *Complex Fluids in Biological Systems: Experiment, Theory, and Computation*, pages 319–355, 2015.

[75] K. Doubrovinski and K. Kruse. Cytoskeletal waves in the absence of molecular motors. *Europhys. Lett.*, 83(1):18003, July 2008.

[76] K. Doubrovinski and K. Kruse. Cell motility resulting from spontaneous polymerization waves. *Phys. Rev. Lett.*, 107(25):258103, December 2011.

[77] W R Holmes, A E Carlsson, and L Edelstein-Keshet. Regimes of wave type patterning driven by refractory actin feedback: transition from static polarization to dynamic wave behaviour. *Phys. Biol.*, 9(4):046005, August 2012.

[78] Edwin Munro, Jeremy Nance, and James R Priess. Cortical flows powered by asymmetrical contraction transport PAR proteins to establish and maintain anterior-posterior polarity in the early *C. elegans* embryo. *Dev. Cell*, 7(3):413–424, 2004.

[79] Yiran Chang and Daniel J. Dickinson. A particle size threshold governs diffusion and segregation of PAR-3 during cell polarization. *Cell Rep.*, 39(2):110652, April 2022.

[80] Stephanie Schonegg and Anthony A. Hyman. CDC-42 and RHO-1 coordinate acto-myosin contractility and PAR protein localization during polarity establishment in *C. elegans* embryos. *Development*, 133(18):3507–3516, September 2006.

[81] Esther Zanin, Arshad Desai, Ina Poser, Yusuke Toyoda, Cordula Andree, Claudia Moebius, Marc Bickle, Barbara Conradt, Alisa Piekny, and Karen Oegema. A conserved RhoGAP limits M phase contractility and coordinates with microtubule asters to confine RhoA during cytokinesis. *Dev. Cell*, 26(5):496–510, 2013.

[82] Konstantin Popov, James Komianos, and Garegin A Papoian. MEDYAN: Mechanochemical simulations of contraction and polarity alignment in actomyosin networks. *PLoS Comput. Biol*, 12(4):e1004877, 2016.

[83] Blaise Delmotte and Florencio Balboa Usabiaga. A scalable method to model large suspensions of colloidal phoretic particles with arbitrary shapes. *J. Comput. Phys.*, 518:113321, December 2024.

[84] Ashwini Krishna, Mariya Savinov, Niv Ierushalmi, Alex Mogilner, and Kinneret Keren. Size-dependent transition from steady contraction to waves in actomyosin networks with turnover. *Nat. Phys.*, 20(1):123–134, January 2024.

[85] Paolo Caldarelli, Alexander Chamolly, Aurélien Villedieu, Olinda Alegria-Prévot, Carole Phan, Jerome Gros, and Francis Corson. Self-organized tissue mechanics underlie embryonic regulation. *Nature*, 633(8031):887–894, September 2024.

[86] Grigorios A Pavliotis and Andrew Stuart. *Multiscale Methods: Averaging and Homogenization*, volume 53. Springer Science & Business Media, 2008.

[87] Nikolai Sergeevich Bakhvalov and Grigory Panasenko. *Homogenisation: Averaging Processes in Periodic Media: Mathematical Problems in the Mechanics of Composite Materials*, volume 36. Springer Science & Business Media, 2012.

[88] Eduard Campillo-Funollet, Chandrasekhar Venkataraman, and Anotida Madzvamuse. Bayesian parameter identification for Turing systems on stationary and evolving domains. *Bull. Math. Biol.*, 81:81–104, 2019.

[89] Alexey Kazarnikov and Heikki Haario. Statistical approach for parameter identification by Turing patterns. *J. Theor. Biol.*, 501:110319, 2020.

[90] David Schnörr and Christoph Schnörr. Learning system parameters from turing patterns. *Mach. Learn.*, 112(9):3151–3190, 2023.

[91] Ruoxi Jiang, Peter Y Lu, Elena Orlova, and Rebecca Willett. Training neural operators to preserve invariant measures of chaotic attractors. *Adv. Neural Inf. Process. Syst.*, 36:27645–27669, 2023.

[92] Kyle Cranmer, Johann Brehmer, and Gilles Louppe. The frontier of simulation-based inference. *Proc. Natl. Acad. Sci. U.S.A.*, 117(48):30055–30062, December 2020.

[93] Michael B. Giles. Multilevel Monte Carlo methods. *Acta Numer.*, 24:259–328, May 2015.

[94] Xiaoyu Wang, Ryan P Kelly, Adrianne L Jenner, David J Warne, and Christopher Drovandi. A comprehensive guide to simulation-based inference in computational biology. *arXiv*, 2409.19675, 2024.

[95] Willem H Hundsdorfer and Jan G Verwer. *Numerical Solution of Time-Dependent Advection-Diffusion-Reaction Equations*, volume 33. Springer, 2003.

[96] Leslie Greengard and June-Yub Lee. Accelerating the nonuniform fast Fourier transform. *SIAM Rev.*, 46(3):443–454, 2004.